# High-throughput Designed and Laser-etched NiFeCrVTi High-entropy Alloys with High Catalytic Activities and Corrosion Resistance for Hydrogen Evolution in Seawater

*Zhaohui Liu, Huanxin Li, Chao Yang,* Min Jiang, Jiao Zhang, Chaopeng Fu**

Z. Liu, C. Yang, M. Jiang, J. Zhang, C. Fu

Shanghai Key Laboratory of Advanced High-temperature Materials and Precision Forming

School of Materials Science and Engineering

Shanghai Jiao Tong University

Shanghai 200240, P. R. China

E-mail: yangchao1987@sjtu.edu.cn; chaopengfu@sjtu.edu.cn

H. Li

Department of Chemistry

Physical & Theoretical Chemistry Laboratory

University of Oxford, South Parks Road

Oxford OX1 3QZ, UK

**Abstract**

Electrocatalytic hydrogen evolution from seawater through wind or solar energy is a cost-effective way to produce green hydrogen fuel. However, the lack of highly active and anti-corrosive electrocatalysts in seawater severely hinders the industrial application. Herein, a novel $Ni_{1.1}FeCr_{0.4}V_{0.3}Ti_{0.3}$ high-entropy alloy was designed through high throughput computing and prepared via powder metallurgy with the surface treated by laser etching under different laser power. The laser-etched NiFeCrVTi high-entropy alloys exhibit a unique periodically ordered structure with multiple active centers and high porosity. The Ni-HEA-30 displays remarkable HER performance with an overpotential of 55.9 mV and a Tafel slope of 47.3 mV $dec^{-1}$ in seawater. DFT calculations are applied to identify the real active sites for HER on the HEA surface as the key factor for both proton and intermediate transformation, which also reveal that the Cr atom promotes the adsorption energy of water molecules and the modulation of the electronic structure plays a crucial role in optimizing the hydrogen binding capabilities of the Ni atoms within the alloy. Additionally, the electrocatalyst displays high corrosion resistance in seawater, contributing to the good durability for hydrogen production. This work uncovers a new paradigm to develop novel electrocatalysts with superior reaction activity in seawater.

## 1. Introduction

The escalating exploitation and consumption of energy have resulted in severe threats to human health and survival, including environmental pollution, global warming, and energy depletion.[1] There is an urgent need to reassess energy strategies and enhance energy conversion efficiency in order to address these pressing challenges. The research on electrocatalytic hydrogen production technology holds immense importance in ensuring energy security and achieving the goal of "double carbon" policy.[2] Electrochemical water-splitting for hydrogen production in a neutral electrolyte offers numerous advantages, including its environmental friendliness, long lifespan, and ability to withstand equipment corrosion in both acidic and alkaline media, ensuring efficient operation.[3] To date, the bottleneck in the field of industrial overall water splitting has been the development of electrocatalytic materials that exhibit high activity and long cycle stability.[4] In this regard, numerous studies have been devoted focusing on the composition selection,[5] structural design,[6] surface modification,[7] and fluid collection assistance,[8] et.al., to develop and explore high-efficiency electrocatalyst electrode.[9] Despite significant progress, the challenge of designing electrocatalytic catalysts with reasonable costs, high current densities, and long cycle stability using abundant metal elements for the commercial production of hydrogen at a scale beyond the laboratory level remains a substantial obstacle. High-entropy materials have gained increased attention across various fields due to their unique microstructures and exceptional mechanical and physicochemical properties. These materials offer advantages such as corrosion resistance even under

severe conditions and the ability to adjust their properties as needed.[10] Since the activities of electrocatalysts are significantly influenced by their composition, structure, and the intermediate species presented on their surfaces, by employing alloying techniques, the adsorption energies of molecules can be adjusted, thereby enhancing the electrocatalytic activity of the catalysts.[11] The successful advancement of high-entropy alloys has paved the way for the development of numerous alternative high-entropy materials that exhibit promising catalytic properties, such as different nonmetallic oxides, nitrides and sulfides.[12] However, the majority of research on high-entropy materials has primarily concentrated on the crystalline solid-solution phase, characterized by a uniformly disordered atomic distribution within the lattice structure. While this approach has yielded valuable insights, it can impose significant restrictions on the potential atomic configurations of the solute metal atoms, thus limiting the range of achievable properties. The field of high-entropy materials still faces significant challenges, particularly regarding the control of atoms with chemically ordered distributions and the identification of atomic configurations that can optimize the desired structural and functional properties. Additionally, while much of the research has focused on acidic or alkaline electrolytes, the study of hydrogen evolution reactions (HER) in neutral or near-neutral electrolytes presents a more complex scenario. This complexity arises due to the involvement of both $H_2O$ molecules and dissociated $H_3O^+$ ions, necessitating further investigation and understanding.

With the advantages of tunable compositions and high stability, high-entropy alloys

(HEAs) have received extensive attention in the field of catalysis in corrosive media.[13] However, only a small part of the vast HEA nanoparticles has been fabricated and utilized in applications in electrocatalysis because of the difficulties in synthesis.[14] In addition, the high entropy materials have been extensively applied in HER, but the majority of these materials still require relatively high overpotentials to achieve the desired current densities, particularly in non-acidic media. Previously, Jia group prepared a FeCoNiAlTi electrode that exhibited an overpotential of 88.2 mV at a current density of 10 mA $cm^{-2}$ in an alkaline solution.[10d] Yao group synthesized CuAlNiMoFe electrode, which exhibited a high overpotential of 183 mV in nonacidic electrolytes.[9c] The relatively high overpotentials for high entropy materials might be ascribed to the following issues: (1) the absence of electroactive sites for water dissociation and improper hydrogen binding energy for H* adsorption and combination;[11a] (2) poor electron transferability/ mass transportability of electrodes which are using insulative polymer binders to maintain electric contact.[15] Therefore, it is necessary to explore novel high entropy electrode materials, especially to accurate identification of active centers, reduce the energy barrier of the intermediate transformation and achieve large-scale industrial application in neutral/near-neutral electrolytes during hydrogen evolution reaction.

Here, a novel and cost-effective high-entropy alloy, namely $Ni_{1.1}FeCr_{0.4}V_{0.3}Ti_{0.3}$ with face-centered cubic (FCC) structure, was designed through high throughput computing and vacuum electric arc melting techniques. Then, the $Ni_{1.1}FeCr_{0.4}V_{0.3}Ti_{0.3}$ (Ni-HEA) alloy surface was subjected to laser etching at varying powers. The

optimized Ni-HEA featured with multiple active centers, abundant porosity, and a reduced binding energy for H* adsorption/desorption, demonstrated remarkable electrocatalytic performance in a neutral environment. The Ni-HEA requires a low overpotential of 37.9 mV (10 mA $cm^{-2}$) and a low Tafel slope of 36.2 mV $dec^{-1}$ in NaCl electrolyte for HER. In the real seawater electrolyte, it needs 55.9 mV (10 mA $cm^{-2}$) and 47.3 mV $dec^{-1}$. DFT calculations provided insights into the active centers of the NiFeCrVTi alloy, demonstrating that the presence of the Cr atom regulated the electronic structure of NiFeCrVTi, the adsorption and dissociation energy of water molecules. The remarkable electrocatalytic performance of Ni-HEA-30 in HER can be attributed to the exceptional synergistic effect of each alloy element and the unique structure created through laser etching. Notably, Ni-HEA-30 surpasses the performance of state-of-the-art nonprecious electrocatalytic materials, further emphasizing its superior capabilities in HER applications.

## 2. Results and Discussion

The elemental combination of Ni, Fe, Cr, V and Ti was chosen due to their high solid solution rate, reasonably high catalyst activity and low cost. Furthermore, Ni and Fe serve as the main active sties, while the presence of the Cr atom influences the adsorption and dissociation energy of water molecules. Additionally, Cr and V can enhance the corrosion resistance, and Ti is incorporated to form the secondary phase. The composition of $Ni_{1.1}FeCr_{0.4}V_{0.3}Ti_{0.3}$ high-entropy alloy was designed and selected from 200 calculated results through high throughput computing by Pandat 2020 software. Here, we present four typical high throughput computing phase diagrams of

calculated NiFeCrVTi compositions as samples (**Figure 1**). Figure 1a shows that the phase diagrams of the NiFeCrVTi with equal atomic ratios. It can be found that its matrix has BCC structure and the secondary phase is Laves phase. The content of the Laves phase is much higher than that of the matrix, suggesting the NiFeCrVTi with equal atomic ratios is very brittle and not easy to be etched. Figure 1b presents the phase diagrams of $Ni_{0.5}Fe_{0.5}Cr_{0.4}V_{0.3}Ti_{0.3.}$ It is clear that the increasing atomic ratios of Ni and Fe lead to the formation of $Ni_3Ti$ phase which can be easily etched by laser. However, the matrix becomes complicated (coexistence of BCC and FCC phases), suggesting the low mechanical and catalytic properties. As the atomic ratios of Ni and Fe further increases, the content of the FCC phase increases and the Laves phase disappears in the matrix of $Ni_{0.8}Fe_{0.5}Cr_{0.4}V_{0.3}Ti_{0.3}$ (Figure 1c). However, the coexistence of BCC and FCC phases and the low content of $Ni_3Ti$ phase suggest the low mechanical and catalytic properties as well. Figure 1d exhibits the optimized elemental composition - $Ni_{1.1}FeCr_{0.4}V_{0.3}Ti_{0.3.}$ It can be found that $Ni_{1.1}FeCr_{0.4}V_{0.3}Ti_{0.3}$ possesses a single FCC structure and higher content of $Ni_3Ti$ phase (compared with that of the $Ni_{0.8}Fe_{0.5}Cr_{0.4}V_{0.3}Ti_{0.3}$) in the temperature range between 450 and 1200 ℃. Therefore, the high throughput computing predicts that $Ni_{1.1}FeCr_{0.4}V_{0.3}Ti_{0.3}$ with the single FCC matrix phase and high content of the desirable $Ni_3Ti$ phase is the best composition. The temperature range of 450-1200 ℃ is useful for the optimization of preparation parameters. The vacuum electric arc melting was employed to fabricate the $Ni_{1.1}FeCr_{0.4}V_{0.3}Ti_{0.3}$ master alloy to prevent elemental segregation. The atomizing equipment was subsequently employed to atomize the master alloy ingots in order to

obtain alloy powders with uniform composition and low impurity. The high heating and cooling rates of SPS processing can contribute to the fine microstructure of solid solution matrix, and micro-size $Ni_3Ti$ precipitates with uniform size and distribution.

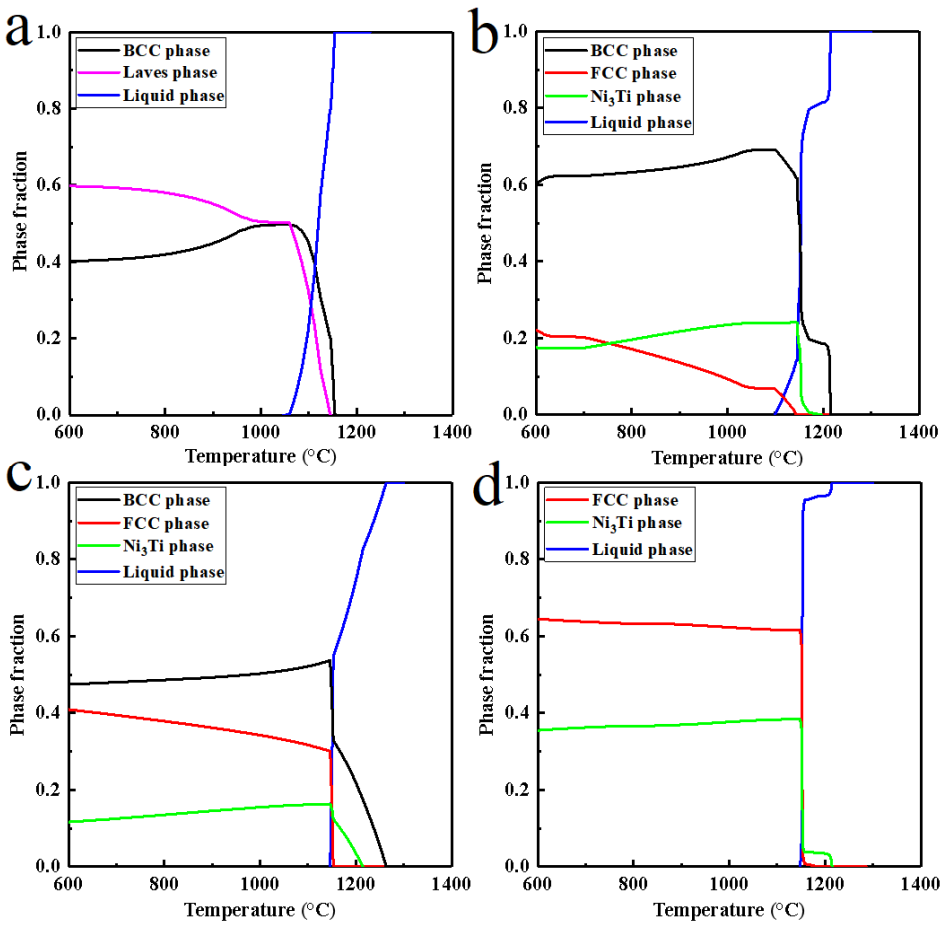


**Figure 1** High throughput computing phase diagrams of (a) NiFeCrVTi, (b) $Ni_{0.5}Fe_{0.5}Cr_{0.4}V_{0.3}Ti_{0.3}$, (c) $Ni_{0.8}Fe_{0.5}Cr_{0.4}V_{0.3}Ti_{0.3}$ and (d) $Ni_{1.1}FeCr_{0.4}V_{0.3}Ti_{0.3}$ high entropy alloys.

The obtained $Ni_{1.1}FeCr_{0.4}V_{0.3}Ti_{0.3}$ was then surface etched by laser at various powers (0, 10, 20, and 30 W) to prepare Ni-HEA-X (X=0, 10, 20 30) samples. By increasing the laser power or extending the etching time, significant changes occur on the surface morphology and structure of the HEA, which are not conducive to improving the hydrogen evolution. **Figure 2**a illustrates the concept behind our

approach. Our hypothesis is that the Ni-HEA-X alloys have the ability to enhance water adsorption while weakening hydrogen adsorption. This unique property promotes the formation of hydronium ions near the catalyst's surface, resulting in fast kinetics during the hydrogen evolution reaction.[7b] Figure 2b displays the XRD diffractograms of Ni-HEA and Ni-HEA-X samples. Among the Ni-HEA-X samples, Ni-HEA-30 was selected as the representative sample due to its similarity in XRD diffractograms to the other Ni-HEA-X samples. It is evident that Ni-HEA comprises a solid-solution FCC phase of Ni, along with a secondary phase of $Ni_3Ti$. However, only the FCC solid-solution Ni phase is present in the Ni-HEA-30 sample. This indicates that the $Ni_3Ti$ secondary phase was effectively removed or etched by the laser treatment using a power of 30 W. Raman spectra were used to monitor the transformation of Ni-HEA before and after laser etching with different powers, and the results are shown in Figure 2c. After laser etching, the Ni-HEA material shows no significant changes in its results. However, Ni-HEA-10, Ni-HEA-20, and Ni-HEA-30 exhibit distinct characteristic peaks in their respective results. The peak at 195 $cm^{-1}$ is attributed to Ti-O,[16] while the peaks around 329 and 753 $cm^{-1}$ could be indexed to the symmetric stretching mode of V-O-V.[17] The peak appearing around 494 $cm^{-1}$ is ascribed to Ni-O,[18] and the broad peak from ~400 to ~700 $cm^{-1}$ represent Ni-O stretch in defective and disordered $Ni(OH)_2$.[19] The obtained results indicate the formation of oxides and hydroxides on the surface of the material through laser etching. This surface modification is expected to be advantageous for the electrocatalytic HER process. As shown in Figure 2d, SEM images indicate that the

Ni-HEA has an uneven surface with pits and includes face-centered cubic (FCC) $Ni_{1.1}FeCr_{0.4}V_{0.3}Ti_{0.3}$ solid solution phase with uniformly distributed face-centered cubic (FCC) $Ni_3Ti$. During laser ablation, the process generates extremely high temperatures and pressures, which are subsequently followed by rapid cooling upon laser irradiation, facilitating the formation and stabilization of the material's morphology. When etched by laser with a power of 10 W, the surface of the high-entropy alloy displayed a lighter regular nick, like a tic-tac-toe shape in Figure S1a, Supporting Information. As the laser power increased to 20 W, the tic-tac-toe shape was more obvious and the surface of Ni-HEA-20 became rougher in Figure S1b, Supporting Information. When the power was as high as 40 W, the unique structure of Ni-HEA was destroyed, so we chose 30 W as the best laser etching power. Figure 2e shows that unlike the concave surface of normal metal plates, the surface of Ni-HEA-30 is composed of rough and porous surface, and the tic-tac-toe shape was observed clearly. Such unique porous architecture not only facilitates electron transfer, but offers high accessibility of the electroactive sites of surface Ni-HEA-30 by virtue of the large channels and the small nanopores. As shown in the representative SEM-EDS elemental mapping (Figure S2, Supporting Information), the Ni, Fe, Cr, V, Ti, and O elements were uniformly distributed along the surface of Ni-HEA-30.

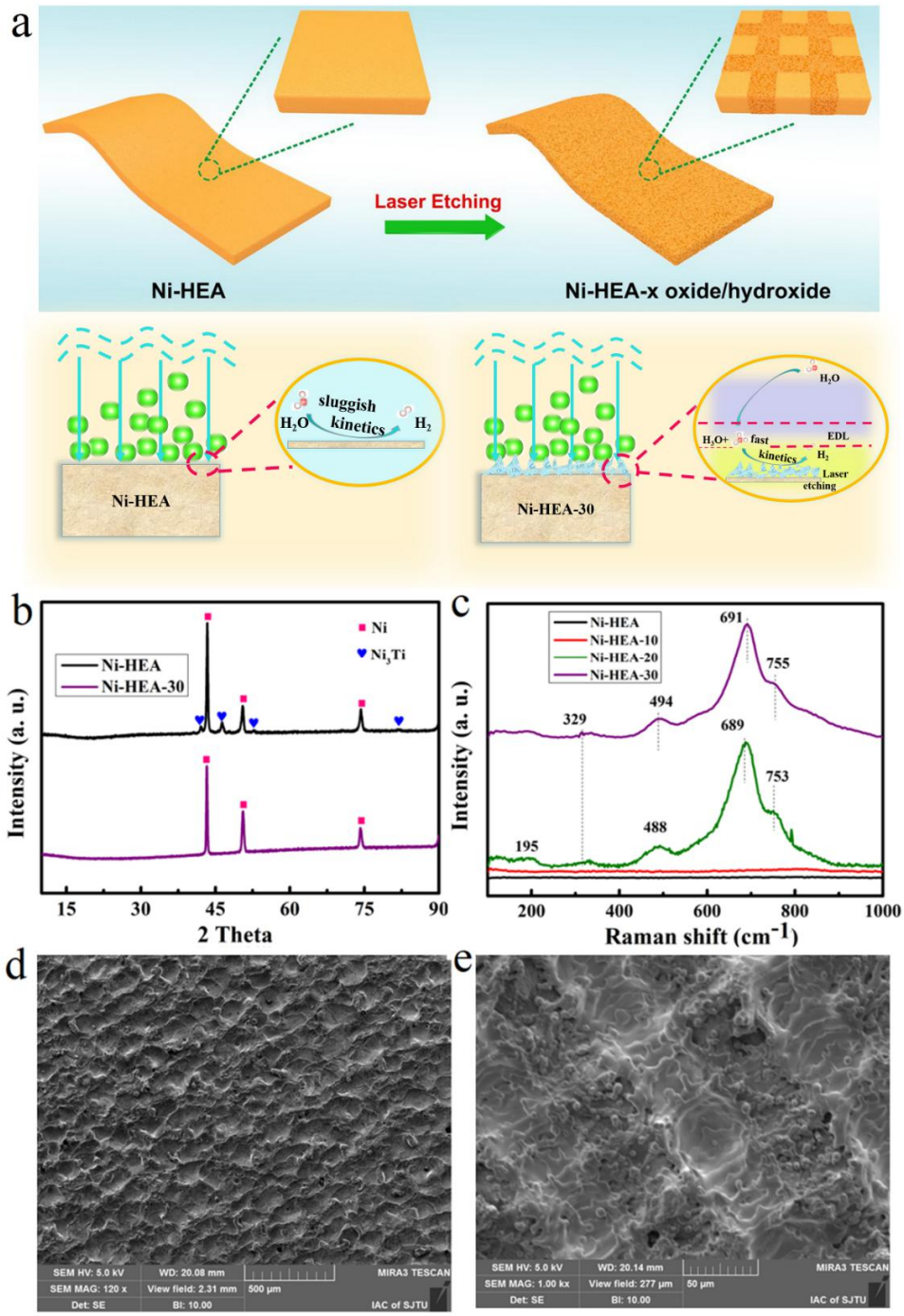


**Figure 2** (a) Schematic illustration of the preparation of Ni-HEA-x and diagram of mass transfer processes mechanism on Ni-HEA, Ni-HEA-30. EDL: electric double layer; (b) XRD patterns of Ni-HEA and Ni-HEA-30; (c) Raman spectrum of the prepared Ni-HEA-X electrodes (d) SEM images of Ni-HEA and (e) Ni-HEA-30.

X-ray photoelectron spectroscopy (XPS) was employed to further analyze the outermost layer of Ni-HEA-X. Given the similarity in the XPS spectra configurations

of Ni-HEA-10, 20, and 30, we have selected Ni-HEA-30 for detailed discussion. The XPS survey spectrum confirms Ni, Fe, V, Cr, Ti, and O in Ni-HEA-30 (Figure S3, Supporting Information). The Ni 2p spectrum of Ni-HEA-30 in **Figure 3**a displays metallic $Ni^0$ $2p_{3/2}$ (852.3 eV) which stems from the Ni-HEA matrix, $Ni^{2+}$ $2p_{3/2}$ (855.3 eV) which originates from $NiO_x$, and a satellite peak Ni $2p_{3/2}$ (860.2 eV) that indicates the oxidation state of nickel is $Ni^{2+/3+}$.[20] The content of $Ni^0$ is lower than the content of $Ni^{2+}$ because of the high chemical activity of Ni.[8a] The Fe 2p spectrum in Figure 3b shows two peaks at 710.5 eV and 723.7 eV which can be attributed to Fe $2p_{3/2}$ and Fe $2p_{1/2}$, respectively, and a little $Fe^0$ peak corresponding to its internal atoms.[9c, 21] In terms of Cr, two characteristic peaks at 576.4 and 573.5 eV can be assigned to $Cr^{3+}$ and metallic $Cr^0$,[20a] respectively (Figure 3c). Figure 3d demonstrates that the peak of Ni-HEA-30 situated at 516.8 eV is indexed to $V^{5+}$ species and the peak at 515.6 eV correspond to $V^{4+}$.[22] Figure 3e presents the high-resolution Ti 2p spectrum of Ni-HEA-30, in which the two peaks at 457.9 and 463.8 eV are assigned to Ti $2p_{3/2}$ and Ti $2p_{1/2}$ orbitals of $Ti^{4+}$.[23] For the oxygen element, as shown in Figure 3f, it is obvious that O 1s peak can be fitted into three peaks at 529.7, 531.2 and 532.2 eV, corresponding to M-O (lattice oxygen species), Ni-O and H-O (hydroxyl species $OH^-$), respectively. The peaks of the O 1s band located at 532.2 eV are attributed to the defects and hydroxyls and chemisorbed oxygen at the surface of the catalysts.[24] These results also indicate that the oxides and hydroxides are formed on the surface of the material by laser etching, which would benefit the electrocatalytic HER process in NaCl electrolyte and seawater.

**Figure 3** XPS spectra of (a) Ni 2p, (b) Fe 2p, (c) Cr 2p, (d) V 2p, (e) Ti 2p, and (f) O 1s.

To evaluate the performance of HER in a neutral electrolyte, we employed the alloy electrodes directly as working electrodes for electrochemical measurements. Initially, the electrocatalytic performance of various samples was evaluated in a 3.5% NaCl solution at room temperature. While all Ni-HEA electrodes possess high conductivity and a unique structure that facilitates electron transfer, it is the Ni-HEA-30 electrode that demonstrates exceptional electrocatalytic performance for neutral HER. This electrode exhibits the lowest overpotentials across various current densities, ranging from 10 to 100 mA $cm^{-2}$. **Figure 4**a illustrates the polarization curves comparing Ni-HEA, Ni-HEA-10, Ni-HEA-20, and Ni-HEA-30 with commercial Pt/C in terms of their performance towards HER. The LSV curve of the Ni-HEA-30 catalyst displays a low overpotential of 37.9 mV at the current density of 10 mA $cm^{-2}$ (normalized to the electrode area), which is far superior to Ni-HEA (485 mV), Ni-HEA-10 (185.2 mV), Ni-HEA-20 (73.9 mV), and close to the performance of Pt/C (17.6 mV). In comparison of Ni-HEA (657 mV), Ni-HEA-10 (275 mV), and Ni-HEA-20 (211 mV), Ni-HEA-30 delivers a low overpotentials of 174 mV at the current densities of 50 mA $cm^{-2}$, and requires a low overpotential of 199 mV at the large current density of 100 mA $cm^{-2}$ towards HER (Figure 4b). The observed enhancement in performance during the electrocatalytic process can be attributed to two possible factors: surface restructuring and the etching of less-stable elements, such as $Ni_3Ti$, from the HEA

catalyst. Figure 4c shows the corresponding Tafel plots of various electrocatalysts. The better activity of Ni-HEA-30 can also be supported by its lower Tafel slope (36.2 mV $dec^{-1}$) than that of Ni-HEA (121.5 mV $dec^{-1}$), Ni-HEA-10 (109.4 mV $dec^{-1}$), Ni-HEA-20 (56.5 mV $dec^{-1}$) and Pt/C (68.7 mV $dec^{-1}$) suggesting the intrinsically distinguished activity and improved catalytic kinetics of Ni-HEA-30, which demonstrates that the Ni-HEA-X catalyst greatly boosts HER kinetics after laser etching. The kinetic process of the HER process could be inferred by the Tafel slope.[25] HER in neutral/near-neutral electrolytes exhibits distinct characteristics compared to strong acidic or alkaline electrolytes. Instead of a single-step reduction (Volmer reaction) process involving $H_3O^+$ ions in strong acidic electrolytes or $H_2O$ molecules in alkaline electrolytes, HER in neutral/near-neutral electrolytes is characterized by diffusion-controlled kinetics at relatively low overpotentials and a switch in reactants from $H_3O^+$ ions to $H_2O$ molecules at high overpotentials. These unique features define the electrochemical behavior of HER in neutral/near-neutral electrolytes.[26] According to the HER kinetics model, the determined theoretical values of Tafel slopes could be divided into three steps: the Volmer (120 mV $dec^{-1}$), Heyrovsky (40 mV $dec^{-1}$), and Tafel reactions (30 mV $dec^{-1}$). The Tafel slopes of approximately 40 mV $dec^{-1}$ for HEA-30 in both NaCl and seawater indicate that the rate-controlling step is the Volmer-Heyrovsky reaction process, whereas others mechanism follow the Volmer-Tafel pathway. This suggests that the mechanism of the HER process in NaCl and seawater is identical.[25] The enhanced HER kinetics

might be attributed to the introduction of oxygen and the synergistic effect between the elements.

In General, the electrochemically active surface areas (ECSAs) is regarded as an estimation of active sites and is proportional to the double-layer capacitance ($C_{dl}$). To better access the catalytic activity of Ni-HEA-X catalysts, their electrochemically active surface area (ECSA) is calculated and used to normalize the currents (Figure S4, Supporting Information). Logically, Ni-HEA-30 shows the highest areal capacitance (1.48 mF $cm^{-2}$), higher than that of Ni-HEA-10 (0.708 mF $cm^{-2}$) and Ni-HEA-20 (0.744 mF $cm^{-2}$). This observation further underscores the advantages of utilizing high-entropy electrocatalysts. Furthermore, it is essential to consider the durability of the electrocatalyst, as it plays a critical role in practical applications. To study the stability of the Ni-HEA-X catalysts in neutral electrolyte, 3000 CV scans were executed. As displayed in Figure S5 and S6, Supporting Information, there is no obviously change of the LSV curves after 3000 cycles, demonstrating the high durability of Ni-HEA-X electrocatalysts in a long-term HER process under neutral conditions. Furthermore, the electronic states of Ni-HEA-X did not significantly change after stability test in NaCl, which were confirmed by XPS in Figure S7 and S8. Considering the aforementioned analysis, it can be inferred that the synergistic effect of alloy atoms and the distinctive morphology plays a crucial role in optimizing charge transfer and catalytic active sites. As a result, the hydrogen evolution reaction (HER) process is significantly enhanced.

To gain a deeper understanding of the practical applicability of Ni-HEA-X as electrocatalysts for the hydrogen evolution reaction (HER), we conducted a series of electrochemical tests in seawater to assess the HER activity and stability of Ni-HEA, Ni-HEA-10, Ni-HEA-20, and a commercially available Pt/C catalyst. As shown in Figure 4d, the Ni-HEA-30 electrocatalysts demonstrated outstanding electrocatalytic activity with a low onset potential. The overpotential of Ni-HEA-30 is 55.9 mV at a current density of 10 mA $cm^{-2}$, while Ni-HEA, Ni-HEA-10, and Ni-HEA-20 exhibited much higher overpotentials of 95.4, 594.5 and 707.2 mV, respectively, but still less active than the commercial Pt/C (32.6 mV). The dramatically reduced overpotential of Ni-HEA-30 reveals the extraordinary HER catalytic activity of high-entropy alloy-based catalysts. The improved HER performance in seawater is contributed by the multi-active centers, abundant porosity and reduced banding energy of H* adsorption/desorption. As shown in Figure 4e, Ni-HEA-30 presents lower overpotentials of 127 mV at the current densities of 50 mA $cm^{-2}$ compared to Ni-HEA (875 mV), Ni-HEA-10 (803 mV) and Ni-HEA-20 (188 mV), and delivers a large current density of 100 mA $cm^{-2}$ at 129 mV. As shown in Figure 4f, the Tafel slopes of Ni-HEA, Ni-HEA-10, Ni-HEA-20, Ni-HEA-30 and Pt/C are 261.9, 242.3, 69.4, 47.3 and 67.8 mV $dec^{-1}$, respectively, which demonstrates that the Ni-HEA-X catalyst greatly boosts HER kinetics in seawater, indicating the short charge transfer length and efficient charge transfer. To better understand the HER performance of the Ni-HEA-X catalysts, we tested the electrochemical double-layer capacitance in Figure S9, Supporting Information. The results show that the electrochemical double-layer

capacitance of Ni-HEA-30 (0.145 mF $cm^{-2}$), higher than that of Ni-HEA-10 (0.064 mF $cm^{-2}$) and Ni-HEA-20 (0.117 mF $cm^{-2}$), indicating that Ni-HEA-30 can expose more active sites. Moreover, the HER activity of all the LSV curves after 3000 cycles, demonstrating the high durability of Ni-HEA-X in a long-term HER process in seawater (Figure S10 and S11, Supporting Information). The XPS analysis reveals that there is no significant structure change of the samples after stability testing (Figure S7 and S12, Supporting Information).

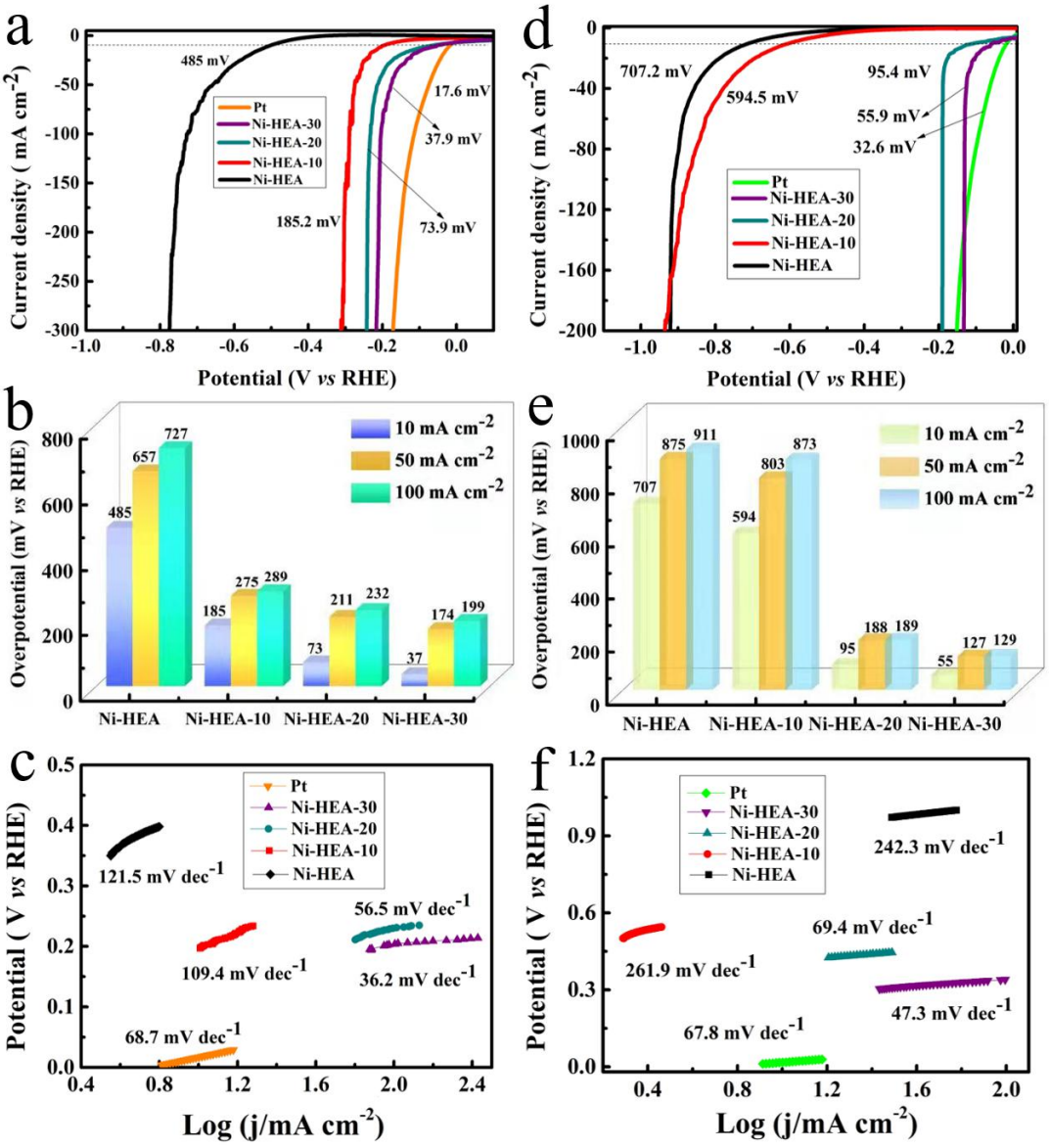

**Figure 4** (a-c) HER catalytic performance in NaCl: (a) HER polarization curves, (b) overpotentials at typical current densities, (c) Tafel slopes of Ni-HEA, Ni-HEA-10, Ni-HEA-20 and Ni-HEA-30; (d-f) HER catalytic performance in seawater: (d) HER polarization curves, (e) overpotentials at typical current densities, (f) Tafel slopes of Ni-HEA, Ni-HEA-10, Ni-HEA-20 and Ni-HEA-30.

The high-entropy alloy electrodes prepared in this study demonstrate outstanding catalytic activity and stability for HER in electrolytes containing chloride ions. To assess the electrocatalyst's resistance against chloride corrosion, we conducted a comprehensive analysis using typical potentiodynamic tests, electrochemical impedance spectroscopy measurements, and open circuit potential tests. These investigations aimed to investigate the corrosion behaviors of Ni-HEA, Ni-HEA-10, Ni-HEA-20, and Ni-HEA-30 in electrolytes containing $Cl^-$ ions. **Figure 5**a shows that the corrosion current in NaCl of Ni-HEA-30 ($4.27\times10^{-7}$ A) is smaller than that of Ni-HEA ($1.239\times10^{-6}$ A), Ni-HEA-10 ($1.061\times10^{-6}$ A) and Ni-HEA-20 ($8.726\times10^{-7}$ A). The corrosion current in seawater (Figure 5b) of Ni-HEA-30 is $1.232\times10^{-6}$ A, which is smaller compared with Ni-HEA ($2.088\times10^{-6}$ A), Ni-HEA-10 ($1.344\times10^{-6}$ A) and Ni-HEA-20 ($1.265\times10^{-6}$ A). The above results demonstrate that Ni-HEA-30 has a higher corrosion resistance than Ni-HEA, Ni-HEA-10, and Ni-HEA-20 in the $Cl^-$ containing electrolyte. Oxygen was induced by the laser etching in this work, leading to the formation of increased Ni/Fe oxides. These oxides layers serve as passive films. The stable open circuit potential (OCP, Figure S13, Supporting Information) value observed in the Ni-HEA-30 sample indicates the formation of a dense and protective

surface passive film. The higher value of OCP is linked to reduced corrosion tendencies, attributed to the presence of a more compact and stable passivation film.[27]

This conclusion is further supported by the impedance results in Figures 5c and S14, Supporting Information, in which the semicircle of the Nyquist plots for Ni-HEA-30 is larger than that of Ni-HEA, Ni-HEA-10, and Ni-HEA-20. Figure 5d shows the good catalytic stability in the HER process, and the stability of the as-prepared electrode was also supported by the OCP results. Meanwhile, according to the previous reports, the higher value of OCP should be attributed to a more compact and stable passivation film.[27a] Compared with Ni-HEA, Ni-HEA-10, and Ni-HEA-20, the chronopotentiometric curves in NaCl (Figure 5e) and in sweater (Figure 5f) of Ni-HEA-30 as an electrode indicate the important role of the metal oxide/hydroxide layer as the actual corrosion-proof layer, which can effectively limit the undesired corrosion caused by the $Cl^-$ participation.

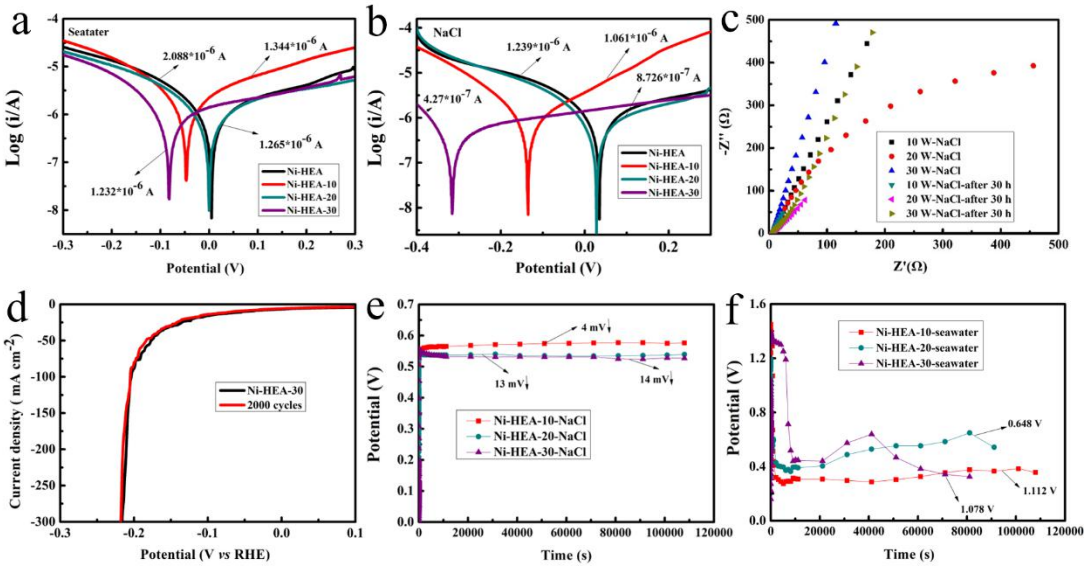

**Figure 5** Tafel plots of Ni-HEA, Ni-HEA-10, Ni-HEA-20 and Ni-HEA-30 (a) in NaCl and (b) in seawater; (c) Electrochemical impedance spectroscopy (EIS) of Ni-HEA, Ni-HEA-10, Ni-HEA-20 and Ni-HEA-30 in NaCl; (d) LSV curves before and after 2000 cycles of Ni-HEA-30; Chronopotentiometric curves of Ni-HEA-10, Ni-HEA-20 and Ni-HEA-30 recorded at a constant cathodic current density of 10 mA $cm^{-2}$ in NaCl (e); and in seawater (f).

It is well-established that the catalytic performance is influenced by the structural configuration and surface composition of the catalyst. Density functional theory (DFT) calculations were conducted to explore the underlying mechanism behind the improved hydrogen evolution reaction (HER) performance of Ni-HEA-30. In this study, laser etching was employed to modify the microstructure and elemental composition on the surface of Ni-HEA. Given that the atomic positions of the elements are randomly occupied, the Monte Carlo method was employed to optimize the distribution state of elements, as illustrated in Figure S15, Supporting Information. Furthermore, the adsorption energy comparison in Figure S16, Supporting Information, revealed that oxygen molecules tend to preferentially adsorb at hollow sites on the metal surface following laser etching.

The Ni-HEA-30 structure with oxygen layers and adsorption of $H_2O$ on the different active sites in **Figure 6**a and Figure S17 and S18, Supporting Information, has been applied due to the highest stability. To deepen our understanding of the electronic structures, we have provided the density of states (DOS) plots for each element in Ni-HEA-30, as shown in Figure S19, Supporting Information. Furthermore,

the corresponding density functional theory (DFT) calculations in Figure 6b and Figure S20, Supporting Information, illustrate that Ni, Fe, Cr, V, and Ti exhibit unique DOS characteristics around the Fermi level. Notably, the Ni-d orbital exhibits a higher electron charge density near $E_V$ -1.306 eV, suggesting that the combination of Ni and oxygen, particularly after the etching process, is likely responsible for enhancing electrical properties and serving as an electron reservoir during reduction processes such as HER.[28] Both Cr-d and Fe-d orbitals dominate the bands near $E_F$, which locate at $E_V$ 0.721 eV and -1.871 eV, respectively. Based on the d-band theory, a lower position of the d-band center most likely results in a weaker binding interaction between the catalysts and adsorbates,[29] which contributes to the enhancement of HER activity of Ni-HEA-30. In the context of the HER, the efficiency of water splitting and subsequent proton transfer relies heavily on the initial adsorption process of water. A more favorable HER reaction occurs when the adsorption energies of $H^+$ are closer to zero, indicating a more favorable proton transfer process.[30] During our calculations, the adsorption/disadsorption energy of $H_2O$ and H at various metal sites on the alloy surface was illustrated in Figure S21 and S22, Supporting Information. As shown in Figure 6c, the calculated $H_2O$ adsorption free energies for Ni-HEA-30 on Cr (-1.10353 eV) and Ni sites (-0.72692 eV) are higher than that on Fe (-0.30574 eV), V (-0.61325 eV) and Ti sites (-0.40321 eV), which activates the dissociation of water molecules. Meanwhile, the Ni and Cr sites show the relatively preferred H* adsorption after the water dissociation, leading to the stabilization of H in the hollow sites surrounded by Ni and Cr. Due to the Cr

atoms possess less 3d orbital electrons, the interaction between Cr and H is very weak H compared with that between Ni and H,[29] thus the actual active sites for hydrogen evolution are Ni sites. Furthermore, to provide insights into the neutral hydrogen evolution reaction (HER) catalytic pathways, we have calculated and presented the energy barriers of the reaction, along with the corresponding structural information, in Figure 6d. It is evident that $H_2O$ exhibits a preference for occupying the active sites of Ni and Fe in Ni-HEA-30, primarily due to the presence of oxidation layers of Ni/Fe-OOH on the surface. The cleavage of HO-H bond goes through a transition state (TS1) with an energy barrier to form an intermediate which with H* on O site and adsorbed OH (HO*) on Ni and Fe sites. The energy barrier on the Fe and Ni active sites dramatically decreases to 1.17 and 1.18 eV, respectively, suggesting that the change of electric charge density could lower the energy barrier of $H_2O$ adsorption and dissociation reaction at interface after laser etching. The HO* prefers to form $OH^-$ that would rapidly migrate from the catalyst surface into the solution in an endothermic manner, leaving the $H_2$* on the catalyst surface. The rate-determining step was observed on the Ni active site with an energy barrier of 0.10 eV, while Fe active site displayed an energy barrier of 0.78 eV. This emphasizes that the presence of heterointerfaces enables the HER catalysis to occur on a significantly lower potential energy surface. Based on the aforementioned results analysis, the presence of Cr in Ni-HEA-30 serves to modulate the electronic structure by shifting the d-band center of Ni atoms further away from the Fermi level. Additionally, the introduction of oxygen atoms through laser etching facilitates the formation of local nickel oxide

and hydroxide species. Notably, NiOOH exhibits a strong binding ability with OH, thereby promoting the dissociation of water and facilitating the production of *H intermediates, ultimately enhancing the hydrogen evolution reaction (HER) activity.[31] The obtained results demonstrate that the Ni-HEA-30 catalyst exhibits a dual enhancement in both the catalytic activity and stability for HER.

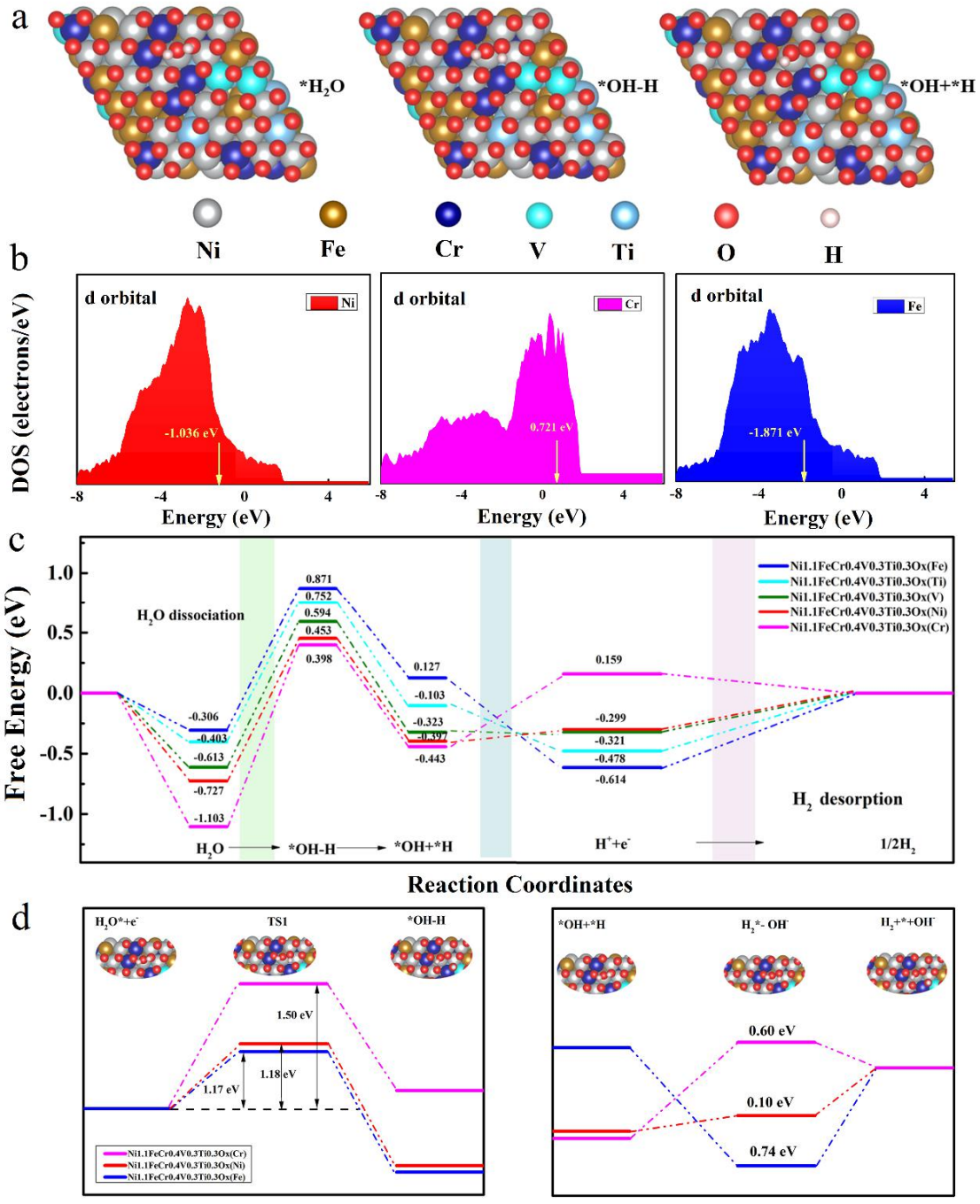


**Figure 6** (a) Schematic shows stable distribution of elements in alloys and adsorption of $H_2O$ on Ni sites of Ni-HEA-30; (b) The projected density-of-states of d orbitals of Ni, Fe and Cr sites with aligned Fermi level in Ni-HEA-30; (c) Free energies of $H_2O$ and H adsorption on various active sites. (d) Rate determining step of Ni, Fe and Cr sites of Ni-HEA-30.

Raman spectroscopy was conducted to investigate the interfacial electrocatalytic behavior of the hydrogen evolution reaction (HER) during the electrochemical process in NaCl (**Figure 7**a) and seawater (Figure 7b). In the presence of NaCl, the Ni-HEA material exhibits no significant changes. However, in the case of Ni-HEA-30, a distinctive peak at approximately 522 $cm^{-1}$ is attributed to the presence of Fe-OH species.[32] The reaction was much more complicated in seawater and the peak at ~841 $cm^{-1}$ was attributed to Cr-OH.[33] For Ni-HEA-X electrocatalysts in Figure 6a and 6b, the peak at ~275 $cm^{-1}$ corresponds to α-$Fe_2O_3$, and the broad peak from ~400 to ~700 $cm^{-1}$ represent Ni-O stretch in defective and disordered $Ni(OH)_2$.[19] Nevertheless, when comparing the Ni-HEA-X electrodes before and after the HER process, a noticeable reduction in the peak intensity within the 200-600 $cm^{-1}$ range is observed. This reduction suggests a phase homogenization and amorphization of the material following the HER test. The remaining strong peak at ~700 $cm^{-1}$ suggests that more octahedral Ni-O structures are produced and such saturated oxygen coordination is known to be beneficial for the electrocatalytic activity.[19, 32] The results of Raman indicate that the active NiOOH and Fe-OH intermediate phases are easier to form during the HER process, which contribute to the electrocatalytic activity. SEM images of Ni-HEA-30 after HER process in NaCl and seawater were also obtained. As can be seen in Figure 7c, the surface of Ni-HEA-30 after electrochemical testing in NaCl still remains the clear tic-tac-toe shape. And the surface was corroded mildly and composed of rough and porous structure (Figure 7d). The surface of Ni-HEA-30 after electrochemical testing in seawater was corroded more seriously than in NaCl, but the

surface morphology was destroyed less significantly and appeared some corrosion products (Figure 7e and 7f). The SEM results indicate the high durability of Ni-HEA-30 in a long-term HER process in NaCl and seawater.

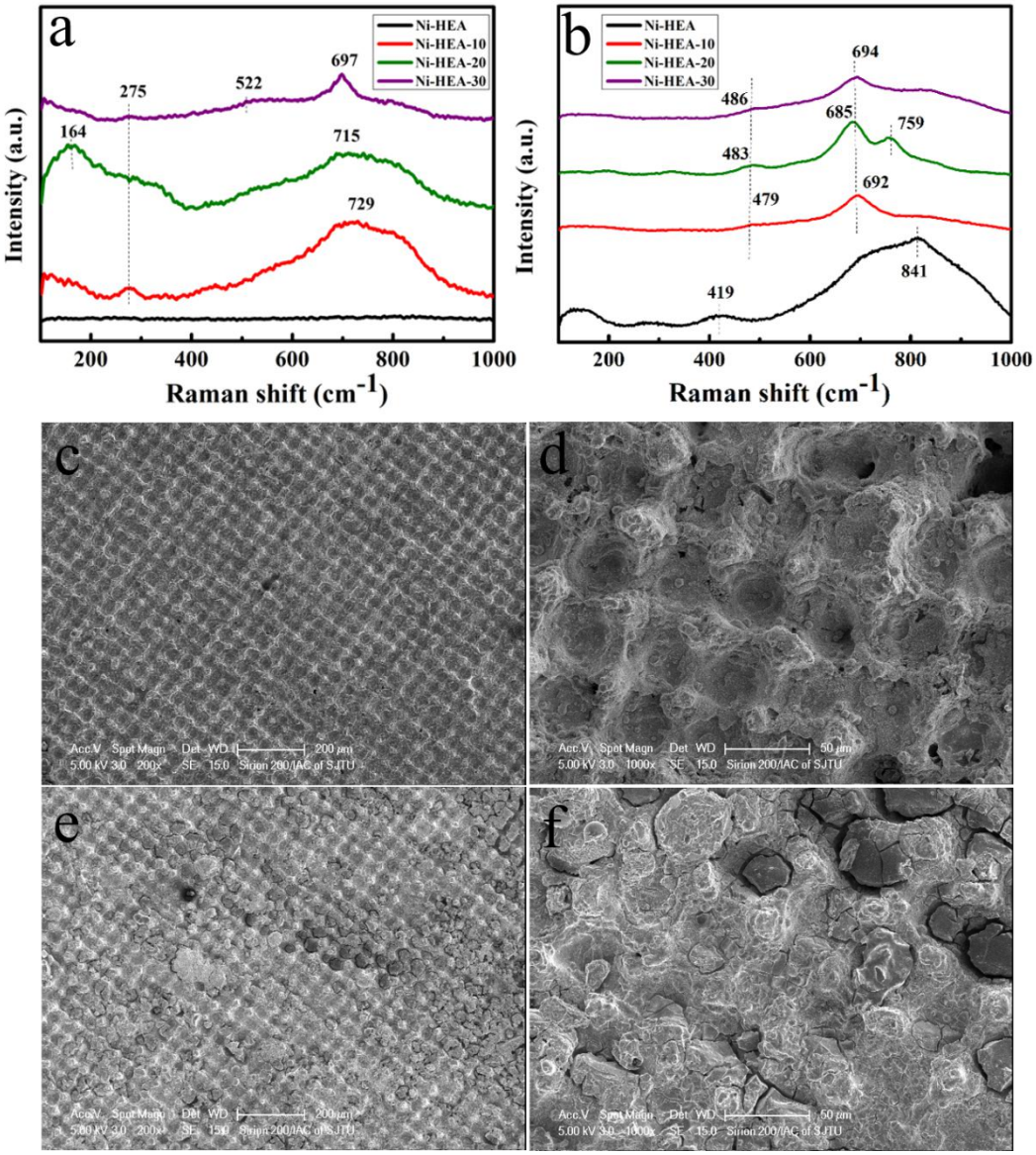


**Figure 7** (a-b) Raman spectroscopy of Ni-HEA-30 after the HER process in different electrolytes: (a) NaCl and (b) seawater; (d-f) SEM images of Ni-HEA-30 after the HER process in different electrolytes: (c-d) NaCl and (e-f) seawater.

## 3. Conclusion

In summary, we designed a novel $Ni_{1.1}FeCr_{0.4}V_{0.3}Ti_{0.3}$ high-entropy alloy (Ni-HEA) via high throughput computing and prepared the non-noble NiFeCrVTi multicomponent alloy employing SPS and laser etching for HER. Both theoretical and experimental approaches were utilized to investigate the catalytic role of this alloy, and we believe that the alloy composition and the morphology work synergistic and have great influence on the electrocatalytic hydrogen evolution. The Ni-HEA-30 variant exhibited exceptional electrocatalytic performance in a neutral environment, including high catalytic activity, stability, and specificity for HER, along with remarkable resistance to chloride corrosion. Ni-HEA-30 demonstrated a low overpotential of 37.9 mV (at 10 mA $cm^{-2}$) for HER and a low Tafel slope of 36.2 mV $dec^{-1}$ in NaCl electrolyte. In seawater, it exhibited even better performance with a lower overpotential of 55.9 mV (at 10 mA $cm^{-2}$) and a lower Tafel slope of 47.3 mV $dec^{-1}$. DFT theoretical calculations revealed that the outstanding HER performance of Ni-HEA-30 can be attributed to the synergistic effect of each alloy element. Notably, the presence of Cr optimized the hydrogen adsorption free energy ($\Delta GH^*$) for efficient electron transfer. Additionally, NiOOH exhibited strong OH binding ability, promoting water dissociation and the production of *H intermediates, which further improved the HER activity. The excellent HER electrocatalytic performance of Ni-HEA-30 can be attributed to the exceptional synergistic effect of each alloy element and the unique structure created by laser etching.

**Supporting Information**

Supporting Information is available from the Wiley Online Library or from the author.

**Acknowledgements**

This work was supported by the National Natural Science Foundation of China (No. 51874197, 51821001, 52304332) and Shanghai Science and Technology Committee (No. 21ZR1429400).

**Conflicts of Interest**

The authors declare no competing financial interest.

**Data Availability Statement**

The data that support the findings of this study are available from the corresponding author upon reasonable request

**Keywords**

electrocatalyst, laser etching, high-entropy alloy, hydrogen evolution reaction

[1] a) Q. W. Zhang, Y. X. Hu, H. F. Wu, X. Y. Zhao, M. Wang, S. Wang, R. Feng, Q. Chen, F. Song, M. Chen, P. Liu, *ACS nano* **2023**, *17,* 1485-1494; b) X. D. Ding, J. Yu, W. Huang, D. Chen, W. Lin, Z. Xie, *Chem. Eng. J.* **2023**, *451*, 138550; c) J. Sielski, K. Kaziród-Wolski, M. A. Józwiak, M. *Sci. Total Environ.* **2021**, *788*, 147541; d) C. P. Wang, Y. X. Lin, L. Cui, J. Zhu, X. H. Bu, *Small* **2023**, *19*, 2207342.

[2] a) Q. Zhang, W. Xiao, W. H. Guo, Y. X. Yang, J. X. Lei, H. Q. Luo, N. B. Li, *Adv. Funct. Mater.* **2021**, *31*, 2102117; b) Y. Z. Li, J. L. Tang, H. L. Zhang, Y. Y. Wang, B. Lin, J. C. Qiao, H. P. Zheng, Z. X. Yu, Y. D. Liu, T. G. Zhou, X. Z. Lei, *Chem. Eng. J.* **2023**, *453*, 139905; c) C. H. Chiang, Y. C. Yang, J. W. Lin, Y. C. Lin, P. T. Chen, C. L. Dong, H. M. Lin, K. M. Chan, Y. T. Kao, K. Suenaga, P. W. Chiu, C. W. Chen, *ACS nano* **2022**, *16*, 18274-18283.

[3] a) G. Bahuguna, A. Cohen, B. Filanovsky, F. Patolsky, *Adv. Sci.* **2022**, *9*, 2203678; b) B. Zhang, J. W. Shan, W. L. Wang, P. Tsiakaras, Y. Y. Li, *Small* **2022**, *18*, 2106012; c) Y.T. Yan, Y. Chen, M. T. Shao, X. Chen, Z. S. Yang, J. M. Wang, H. Y. Chen, L. B. Ni, G. W. Diao, M. Chen, *ACS Sustainable Chem. Eng.* **2023**, *11*, 2499-2510.

[4] a) L. Dai, Z. N. Chen, L. Li, P. Yin, Z. Liu, H. Zhang, *Adv. Mater.* **2020**, *32*, 1906915; b) C. L. Huang, Y. G. Lin, C. L. Chiang, C. K. Peng, D. S. Raja, C. T. Hsieh, Y. A. Chen, S. Q. Chang, Y. X. Yeh, S. Y. Lu, *Appl. Catal. B: Environ.* **2023**, *320*, 122016; c) X. Zhang, M. T. Zhang, Y. C. Deng, M. Q. Xu, L. Artiglia, W. Wen, R. Gao, B. B. Chen, S. Y. Yao, X. C. Zhang, M. Peng, J. Yan, A. Li, Z. Jiang, X. Y. Gao, S. F. Cao, C. Yang, A. J. Kropf, J. N. Shi, J. L. Xie, M. S. Bi, A. Jeroen, V. Bokhoven, Y. W. Li, X. D. Wen, M. F. Stephanopoulos, C. Shi, W. Zhou, D. Ma, *Nature* **2021**, *589*, 396-401.

[5] a) N. S. Gultom, T. S. Chen, M. Z. Silitonga, D. H. Kuo, *Appl. Catal. B: Environ.* **2023**, *322*, 122103; b) Z. H. Zhang, X. H. Liu, D. Wang, H. Wan, Y. Zhang, G. Chen, N. Zhang, R. Z. Ma, *Chem. Eng. J.* **2022**, *446*, 137037; c) Y. Mu, Y. F.

Zhang, Z. Y. Feng, X. Y. Dong, X. Y. Jing, X. Y. Pei, Y. F. Zhao, Z. K. Kou, C. G. Meng, *Chem. Eng. J.* **2023**, *460*, 141709.

[6] a) X. Yang, J. Cheng, X. Yang, Y. Xu, W. F. Sun, J. H. Zhou, *Chem. Eng. J.* **2023**, *451*, 138977; b) T. Dong, X. Zhang, P. Wang, H. S. Chen, P. Yang, *Electrochim. Acta* **2020**, *338*, 135885; c) Y. Zhang, H. Guo, X. Li, J. Du, W. Ren, R. Song, *Chem. Eng. J.* **2021**, *404*, 126483; d) T. Y. Gong, J. Y. Zhang, Y. Liu, L. R. Hou, J. L. Deng, C. Z. Yuan, *Chem. Eng. J.* **2023**, *451*, 139025.

[7] a) C. Y. Jian, W. T. Hong, Q. Cai, J. Li, W. Liu, *Appl. Catal. B: Environ.* **2020**, *266*, 118649; b) H. Y. Jin, X. S. Wang, C. Tang, A. Vasileff, L. Q. Li, A. Slattery, S. Z. Qiao, *Adv. Mater.* **2021**, *33*, 2007508; c) X. P. Sun, P. Wei, S. Q. Gu, J. X. Zhang, Z. Jiang, J. Wan, Z. Y. Chen, L. Huang, Y. Xu, C. Fang, Q. Li, J. T. Han, Y. H. Huang, *Small* **2020**, *16*, 1906057; d) D. W. Wang, Y. T. Chen, L. B. Fan, T. Xiao, T. Meng, Z. C. Xing, X. R. Yang, *Appl. Catal. B: Environ.* **2022**, *305*, 121081.

[8] a) H. D. Li, Y. Han, H. Zhao, W. J. Qi, D. Zhang, Y. D. Yu, W. W. Cai, S. X. Li, J. P. Lai, B. L. Huang, L. Wang, *Nat. commun.* **2020**, *11*, 1-9; b) J. Y. Xu, I. Amorim, Y. Li, J. J. Li, Z. P. Yu, B. S. Zhang, A. Araujo, N. Zhang, L. F. Liu, *Carbon Energy* **2020**, *2*, 646-655.

[9] a) Liu, H.; H. Y. Qin, J. L. Kang, L. Y. Ma, G. X. Chen, Q. Huang, Z. J. Zhang, H. M. Lu, J. X. Li, N. Q. Zhao, *Chem. Eng. J.* **2022**, *435*, 134898; b) H. Shi, X. Y. Sun, Y. Liu, S. P. Zeng, Q. H. Zhang, L. Gu, T. H. Wang, G. F. Han, Z. Wen, Q. R. Fang, X. Y. Lang, Q. Jiang, *Adv. Funct. Mater.* **2023**, *33*, 2214412; c) R. Q.

Yao, Y. T. Zhou, H. Shi, W. B. Wan, Q. H. Zhang, L. Gu, Y. F. Zhu, Z. Wen, X. Y. Lang, Q. Jiang, *Adv. Funct. Mater.* **2021**, *31*, 2009613; d) K. Xiao, J. X. Wei, W. K. Han, Z. Q. Liu, *J. Power Sources* **2021**, *487*, 229408.

[10] a) Z. J. Zhang, M. M. Mao, J. W. Wang, B. Gludovatz, Z. Zhang, Scott X. Mao, Easo P. George, Q. Yu, *Nat. commun.* **2015**, *6*, 1-6; b) Z. W. Wang, I. Baker, W. Guo, J. D. Poplawsky, *Acta Mater.* **2017**, *126*, 346-360; c) D. B. Miracle, O. N. Senkov, *Acta Mater.* **2017**, *122*, 448-511; d) Z. Jia, T. Yang, L. G. Sun, Y. L. Zhao, W. P. Li, J. H. Luan, F. Lyu, L. C. Zhang, J. J. Kruzic, J. J. Kai, J. C. Huang, J. Lu, Chain T. Liu, *Adv. Mater.* **2020**, *32*, 2000385.

[11] a) T. A. A. Batchelor, J. K. Pedersen, S. H. Winther, I. E. Castelli, K. W. Jacobsen, J. Rossmeis, *Joule* **2019**, *3*, 834-845; b) F. Lv, W. Y. Zhang, W. X. Yang, J. R. Feng, K. Wang, J.H. Zhou, P. Zhou, S. J. Guo, *Small Methods* **2020**, *4*, 1900129.

[12] a) Q. S. Wang, A. Sarkar, D. Wang, L. Velasco, R. Azmi, S. S. Bhattacharya, T. Bergfeldt, A. Du¨vel, P. Heitjans, T. Brezesinski, H. Hahn, B. Breitung, *Energy Environ. Sci.* **2019**, *12*, 2433-2442; b) T. Jin, X. H. Sang, R. R. Unocic, R. T. Kinch, X. F. Liu, J. Hu, H. L. Liu, S. Dai, *Adv. Mater.* **2018**, *30*, 1707512; c) Zhang, R. Z.; Gucci, F.; Zhu, H. Y.; Chen, K.; Reece, M. J. *Inorg. Chem.* **2018**, *57*, 13027-13033.

[13] a) R. Q. Yao, Y. T. Zhou, H. Shi, W. B. Wan, Q. H. Zhang, L. Gu, Y. F. Zhu, Z. Wen, X. Y. Lang, Q. Jiang, *Adv. Funct. Mater.* **2021**, *31*, 2009613; b) D. Zhang, H. Zhao, X. K. Wu, Y. Deng, Z. C. Wang, Y. Han, H. D. Li, Y. Shi, X. L. Chen,

S. X. Li, J. P. Lai, B. L. Huang, L. Wang, *Adv. Funct. Mater.* **2021**, *31*, 2006939; c) H. D. Li, M. Z. Sun, Y. Pan, J. Xiong, H. Y. Du, Y. D. Yu, S. H. Feng, Z. J. Li, J. P. Lai, B. L. Huang, L. Wang, *Appl. Catal. B: Environ.* **2022**, *312*, 121431; d) H. D. Li, J. P. Lai, Z. J. Li, L. Wang, *Adv. Funct. Mater.* **2021**, *31*, 2106715.

[14] D. S. Wu, K. Kusada, Y. Nanba, M. Koyama, T. Yamamoto, T. Toriyama, S. Matsumura, O. Seo, I. Gueye, J. Kim, L. Singgapulige, R. Kumara, O. Sakata, S. Kawaguchi, Y. Kubota, H. Kitagawa, *J. Am. Chem. Soc.* **2022**, *144*, 3365-3369.

[15] C. Panda, P. W. Menezes, M. Zheng, S. Orthmann, M. Driess, *ACS Energy Lett.* **2019**, *4*, 747-754.

[16] Z. Wu, X. Q. Liu, C. Yu, F. Li, W. Q. Zhou, L. F. Wei, *Sci. Total Environ.* **2021**, *796*, 148941.

[17] R. L. Frost, S. J. Palmer, J. Čejka, J. Sejkora, J. Pl´aˇsil, S. Bahfennea, E. C. Keeffe, *J. Raman Spectrosc.* **2011**, *42*, 1701-1710.

[18] A. Bhatia, Y. D. Zrelli, J. P. Pereira-Ramos, R. Baddour-Hadjean, *J. Mater. Chem. A* **2021**, *9*, 13496-13505.

[19] X. Bo, Y. B. Li, X. J. Chen, C. Zhao, *Chem. Mater.* **2020**, *32*, 4303-4311.

[20] a) Z. J. Chen, T. Zhang, X. Y. Gao, Y. J. Huang, X. H. Qin, Y. F. Wang, K. Zhao, X. Peng, C. Zhang, L. Liu, M. H. Zeng, H. B. Yu, *Adv. Mater.* **2021**, *33*, 2101845; b) X. Bo, Y. B. Li, R. K. Hocking, C. Zhao, *ACS appl. Mate. interfaces* **2017**, *9*, 41239-41245.

[21] X. F. Lu, L. Yu, X. W. Lou, *Sci. Adv.* **2019**, *5*, eaav6009.

[22] N. Zhang, Y. Dong, M. Jia, X. Bian, Y. Y. Wang, M. D. Qiu, J. Z. Xu, Y. C. Liu,

L. F. Jiao, F. Y. Cheng, *ACS Energy Lett.* **2018**, *3*, 1366-1372.

[23] a) T. W. Wu, H. T. Zhao, X. J. Zhu, Z. Xing, Q. Liu, T. Liu, S. Y. Gao, S. Y. Lu, G. Chen, Abdullah M. Asiri, Y. N. Zhang, X. P. Sun, *Adv. Mater.* **2020**, *32*, 2000299; b) M. Zhang, Y. Wang, Y. Y. Zhang, J. Song, Y. Si, J. H. Yan, C. L. Ma, Y. T. Liu, J. Y. Yu, B. Ding, *Angew. Chem. Int. Edit.* **2020**, *59*, 23252-23260.

[24] [22] a) S. Peng, F. Gong, L. Li, D. Yu, D. Ji, T. Zhang, Z. Hu, Z. Zhang, S. Chou, Y. Du, S. Ramakrishna, *J. Am. Chem. Soc.* **2018**, *140*, 13644-13653; b) T. Q. Yu, Q. L. Xu, L. Luo, C. R. Liu, S. B. Yin, *Chem. Eng. J.* **2022**, *430*, 133117.

[25] S. Q. Wang, B. L. Xu, W. Y. Huo, H. C. Feng, X. F. Zhou, F. Fang, Z. H. Xie, J. K. Shang, J. Q. Jiang, *Appl. Catal. B: Environ.* **2022**, *313*, 121472.

[26] Z. Zhou, Z. G. Pei, L. Wei, S. L. Zhao, X. Jian, Y. Chen, *Energy Environ. Sci.* **2020**, *13*, 3185-3206.

[27] a) J. H. Li, Y. P. Liu, H. Chen, Z. K. Zhang, X. X. Zou, *Adv. Funct. Mater.* **2021**, *31*, 2101820; b) Z. J. Zheng, Y. Gao, Y. Gui, M. Zhu, *Corros. Sci.* **2012**, *54*, 60-67.

[28] S. C. Zhang, W. B. Wang, F. L. Hu, Y. Mi, S. Z. Wang, Y. W. Liu, X. M. Ai, J. K. Fang, H. Q. Li, T. Y. Zhai, *Nano-Micro Lett.* **2020**, *12*, 1-16.

[29] N. Yao, P. Li, Z. R. Zhou, Y. M. Zhao, G. Z. Cheng, S. L. Chen, W. Luo, *Adv. Energy Mater.* **2019**, *9*, 1902449.

[30] Y. Lu, K. Huang, X. Cao, L. Y. Zhang, T. Wang, D. D. Peng, B. W. Zhang, Z. Liu, J. S. Wu, Y. Zhang, C. J. Chen, Y. Z. Huang, *Adv. Funct. Mater.* **2022**, *32*,

2110645.

[31] a) L. Zhao, Y. Zhang, Z. L. Zhao, Q. H. Zhang, L. B. Huang, L. Gu, G. Lu, J. S. Hu, L. J. Wan, *Natl. Sci. Rev.* **2020**, *7*, 27-36; b) J. S. Wang, S. S. Xin, Y. Xiao, Z. F. Zhang, Z. M. Li, W. Zhang, C. J. Li, R. Bao, J. Peng, J. H. Yi, S. L. Chou, *Angew. Chem. Int. Edit.* **2022**, *61*, e202202518.

[32] X. D. Cheng, J. X. Yuan, J. H. Cao, C. J. Lei, B. Yang, Z. J. Li, X. G. Zhang, C. Yuan, L. C. Lei, Y. Hou, *J. Colloid Interf. Sci.* **2020**, *579*, 340-346.

[33] A. S. O. Gomes, N. Yaghini, A. Martinelli, E. Ahlbergc, *J. Raman Spectrosc.* **2017**, *48*, 1256-1263.